Letter

Determination of the crystal structures of $NdBaMn_2O_6$: Coexisting polar and nonpolar phases

Md Shafiqul Islam,[1,2,*] Daisuke Morikawa,[1] Shigeki Yamada,[3] Bikas Aryal,[1,2] Kenji Tsuda,[1,2] and Masami Terauchi[1]

[1]*Institute of Multidisciplinary Research for Advanced Materials, Tohoku University, 2-1-1 Katahira, Aoba-ku, Sendai 980-8577, Japan*

[2]*Frontier Research Institute for Interdisciplinary Sciences, Tohoku University, Aramaki aza Aoba 6-3, Aoba-ku, Sendai 980-8578, Japan*

[3]*Department of Materials System Science, Yokohama City University, Yokohama 236-0027, Japan*

(Received 21 November 2022; revised 9 July 2023; accepted 15 August 2023; published 25 August 2023)

The crystal structures of coexisting polar and nonpolar phases in *A*-site ordered $NdBaMn_2O_6$ were investigated by a combination of convergent-beam electron diffraction (CBED) and density functional theory (DFT) calculations. A symmetry analysis of the CBED patterns from several segments of *A*-site ordered $NdBaMn_2O_6$ at room temperature (RT $\approx$ 293 K) revealed the presence of two crystallographic distinct phases with polar *C*2*mm* (No. 38) and nonpolar *Cmmm* (No. 65) space groups. The combined method was used successfully to determine the crystal structures of the coexisting phases with the same chemical composition and similar lattice parameters. DFT calculations revealed that the comparable total energies of the two phases could be the origin of their coexistence.

DOI: 10.1103/PhysRevB.108.L060104

The determination of crystal structures at the atomic level is critical for understanding the functionality of newly synthesized materials. The materials can be polar or nonpolar depending on the charge distribution and structural geometry. Polar structures, in contrast to nonpolar structures, have received considerable attention in material science and engineering because of their technologically significant features such as piezoelectricity, pyroelectricity, ferroelectricity, and second-order nonlinear optical properties [1–3]. Consequently, characterizing the polar and nonpolar structures using structure analysis methods such as x-ray diffraction (XRD) and electron diffraction (ED) is critical.

XRD is one of the most commonly used methods for the determination of the crystal structure. As the method is based on the kinematical diffraction theory, it follows Friedel's law, which states that hkl and $\bar{h}\bar{k}\bar{l}$ reflections have the same intensity for both polar and nonpolar structures. To identify the polar structure, the anomalous scattering effect is included in the XRD structure refinement [4–6]. One of the difficult cases for the XRD is when polar and nonpolar structural phases coexist in a material with domain sizes of less than 100 μm, the same chemical composition, and almost the same lattice parameters. Then, a precise identification of coexisting polar and nonpolar structures would be challenging because of the overlapping of the diffraction peaks [7]. Therefore, it is essential to adopt an effective method for examining the coexistence of polar and nonpolar structural phases with the same chemical composition and similar lattice parameters.

Convergent-beam electron diffraction (CBED), which is entirely based on dynamical diffraction, can distinguish between polar and nonpolar structures [8–11]. However, the CBED method requires an initial model structure to refine the crystal structure. To obtain an initial model structure, an application of first-principles calculations based on density functional theory (DFT) can be a reasonable solution. Depending on the determined space group symmetry, the DFT calculations can predict several possible stable geometries of an unknown structure [12].

In recent years, *A*-site ordered perovskite-type manganites, $RBaMn_2O_6$ (R = Y and rare-earth elements), have drawn considerable attention due to their rich phase diagram [13–16]. Unlike other *A*-site ordered perovskite-type manganites, the position of $NdBaMn_2O_6$ (R = Nd) is on the phase boundary, where two structural groups with tilting and no tilting of the octahedra compete with each other [14,16]. So far, there is still controversy about the polar and nonpolar structure of $NdBaMn_2O_6$ at the room temperature (RT) phase [17–19]. The reason for the controversy may be structural coexistence, as $NdBaMn_2O_6$ is located near the phase boundary. In this Letter, the coexistence of polar and nonpolar phases in $NdBaMn_2O_6$ at RT ($\approx$293 K) has been investigated using the combined method of the CBED and DFT calculations.

Single-crystalline bulk specimens of $NdBaMn_2O_6$ were synthesized using the floating zone technique [17]. For transmission electron microscopy (TEM), specimens were prepared by crushing bulk single crystals and gluing small segments to the copper grids. The size of each segment was approximately 10–100 μm. CBED patterns were obtained from different specimen areas within each segment. In this study, 20 segments were examined using an energy filtered TEM JEM-2010FEF, which was operated at a nominal accelerating voltage of 100 kV. The TEM JEM-2010FEF is equipped with a field-emission gun and an in-column Ω-type energy filter. The size of the electron probe is approximately 1 nm in diameter.

To investigate the coexistence of two structural phases, a total energy calculation and structure optimization were performed using a first-principles method based on DFT [20–22] as implemented in the plane-wave self-consistent field (PWSCF) codes within the QUANTUM ESPRESSO simulation package [12,23]. Since an equivalent set of k points is essen-

*islam.md.shafiqul.c6@tohoku.ac.jp

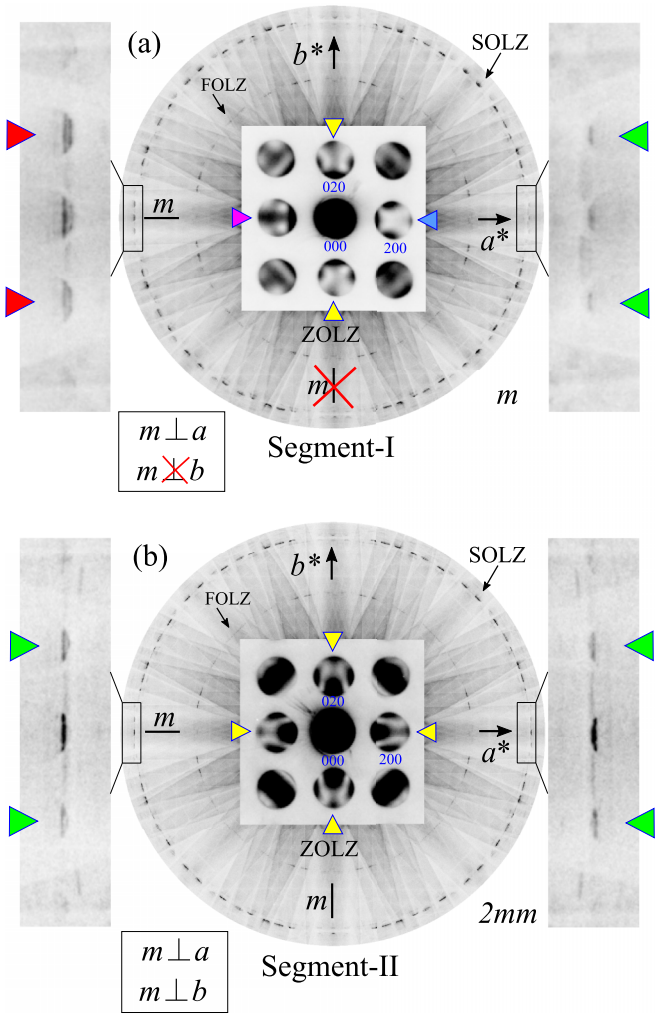

FIG. 1. CBED patterns at [001] incidence taken from (a) segment I [19] and (b) segment II. Here, *m* indicates the mirror symmetry parallel to electron incidence. In the ZOLZ pattern, the magenta and blue arrowheads in (a) represent the reflection disks opposing mirror symmetry, whereas the yellow arrowheads in (b) represent the reflection disks having mirror symmetry. In the SOLZ pattern, the red and green arrowheads in (a) represent the reflection lacking mirror symmetry, whereas the green arrowheads in (b) represent the reflection disks keeping mirror symmetry.

tial to accurately compare the total energies of the structures, Brillouin zone sampling was performed using the Monkhorst-Pack scheme [24] with a $4 \times 4 \times 4$ k-point mesh for both structural phases. The remaining calculation conditions were kept the same as in Ref. [19]. The best-optimized structure for each structural phase was selected by conducting a qualitative comparison of experimental and simulated CBED patterns with [001], [100], and [010] incidences. To simulate the CBED patterns, many-beam dynamical calculations were performed using the optimized structures, structure factors from the independent atom model, and estimated values of atomic displacement parameters (the details of the estimation are shown in Table S1 in the Supplemental Material [25]), as implemented in the MBFIT simulation package [26–28]. In principle, the higher-order Laue zone (HOLZ) reflections,

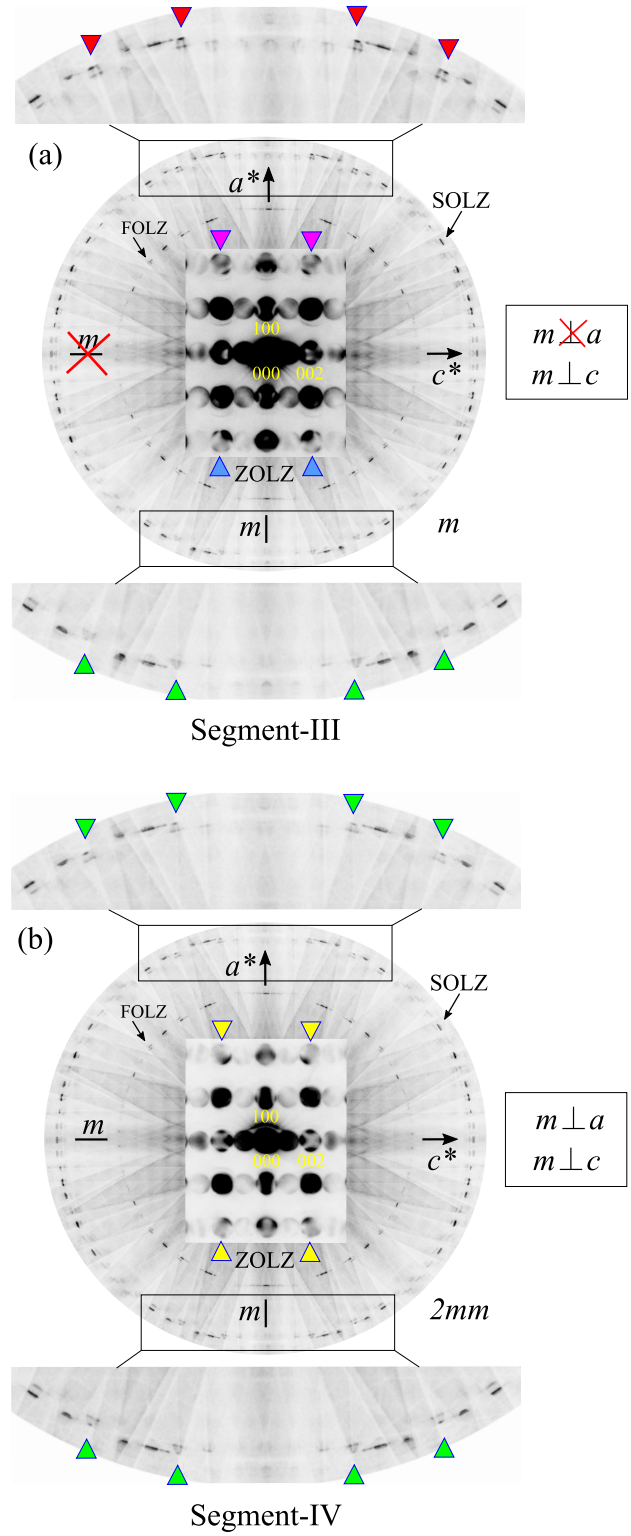

FIG. 2. CBED patterns at [010] incidence taken from (a) segment III and (b) segment IV. Here, *m* indicates the mirror symmetry parallel to electron incidence. In the ZOLZ pattern, the magenta and blue arrowheads in (a) represent the reflection disks lacking mirror symmetry, whereas the yellow arrowheads in (b) indicate the reflection disks having mirror symmetry. In the SOLZ pattern, the red and green arrowheads in (a) ensure the absence of mirror symmetry perpendicular to the *a* axis, whereas the enlarged SOLZ pattern in (b) shows the presence of 2*mm* symmetry.

such as the first-order Laue zone (FOLZ) and second-order Laue zone (SOLZ) reflections, have larger reciprocal lattice vectors **g** than zeroth-order Laue zone (ZOLZ) reflections. Owing to the large **g** vector, the intensities of the HOLZ reflections are more sensitive to small atomic displacements than the ZOLZ reflections [26,27]. Consequently, the HOLZ reflections can be used to distinguish between two structures with a small difference in atomic positions. To compare the simulated and experimental CBED patterns, the position and tendency of the intensity distribution inside the HOLZ reflection disks were visually checked.

To investigate the RT phase, more than 300 CBED patterns were obtained from different areas of 20 segments and categorized based on their symmetry. In order to better understand the experimental CBED patterns, a schematic representation of the CBED pattern is briefly explained in Fig. S1 [25]. Figure 1 shows the CBED patterns at [001] incidence obtained from segment I and segment II. Figure 2 shows the CBED patterns at [010] incidence obtained from two different areas A1 and A2 of segment III. The TEM images of the segments with [001] and [010] incidences and corresponding selected-area electron diffraction (SAED) patterns are shown in Figs. S2 and S3 [25]. According to the obtained SAED patterns from several segments at [001], [010], and [100] incidences, the lattice type is determined to be *C* centered by the extinction condition $hk0 = 2n + 1$, where n is an integer. All of the reflections are indexed by assuming an orthorhombic unit cell with dimensions of $2a_{pc} \times 2b_{pc} \times 2c_{pc}$, where a_{pc}, b_{pc}, and c_{pc} indicate the lattice parameters of the pseudocubic perovskite structure. In the CBED pattern at [001] incidence as shown in Fig. 1(a), the ZOLZ pattern is observed in the center which is extended with a different contrast, whereas the HOLZ reflections, such as FOLZ and SOLZ reflections, appear as ring-shaped diffraction intensities surrounding the ZOLZ reflections. Both the ZOLZ and SOLZ reflections in Fig. 1(a) exhibit a mirror symmetry perpendicular to the *b* axis and mirror symmetry breakdown perpendicular to the *a* axis. Compared with the zone-axis CBED pattern, the existence of mirror symmetry is much more robust in the tilted CBED pattern. To ensure the symmetry of each incidence, the CBED patterns are taken with a slight tilt, as shown in Figs. S4–S7 [25]. From the observation of the zone-axis and tilted CBED patterns of segment I, it is evident that there is no mirror symmetry perpendicular to the *a* axis. By contrast, the CBED pattern in Fig. 1(b) clearly shows 2*mm* symmetry, two mirror symmetries perpendicular to the *b* axis and the *a* axis. The symmetry breakdown perpendicular to the *a* axis of the CBED pattern is not owing to the surface normal issue, as explained in Figs. S8 and S9 [25].

The CBED pattern at [010] incidence as shown in Fig. 2(a) exhibits the absence of mirror symmetry perpendicular to the *a* axis. By contrast, the ZOLZ and SOLZ reflections exhibit

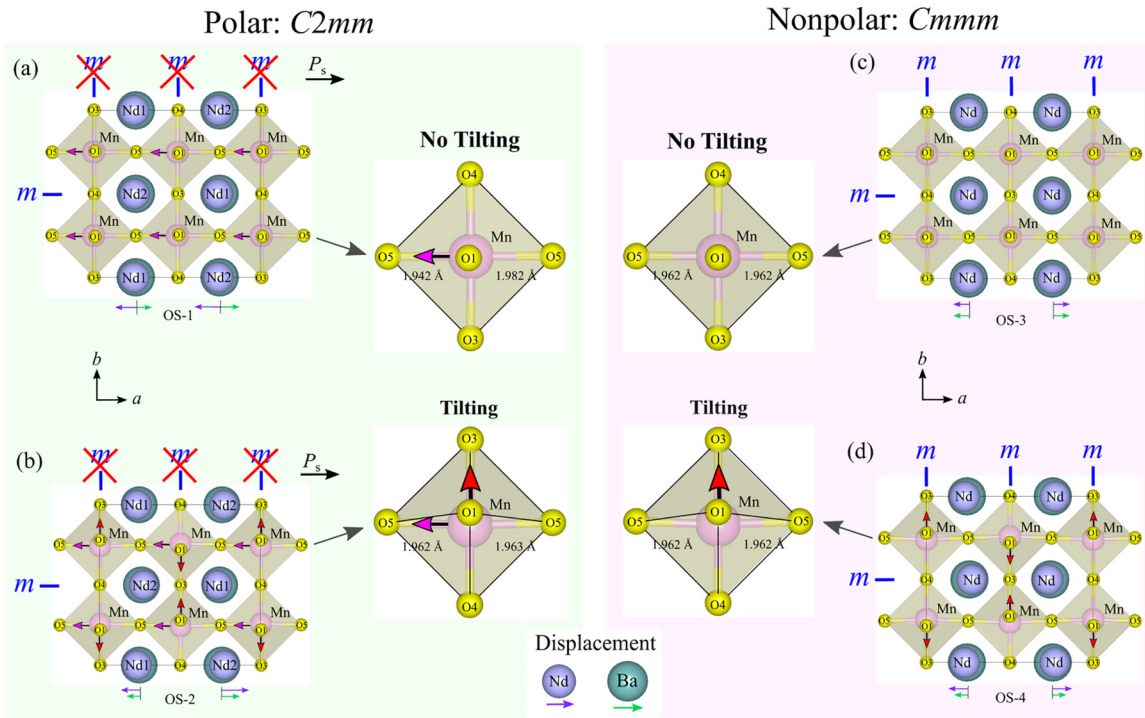

FIG. 3. Unit cells of possible optimized crystal structures of $NdBaMn_2O_6$ at RT viewed from the *a*-axis direction. Two possible optimized structures of the *C*2*mm* phase: (a) Optimized structure OS-1 exhibiting almost no octahedra tilting around the *a* axis, and (b) optimized structure OS-2 exhibiting alternative octahedra tilting around the *a* axis. Here, the magenta arrows indicate the shifting of the Mn atom along the *a* axis and the black arrow on the projected structure indicates the possible direction of the spontaneous polarization (P_s). Two possible optimized structures of the *Cmmm* phase: (c) Optimized structure OS-3 with almost no octahedra tilting around the *a* axis, and (d) optimized structure OS-4 with alternative octahedra tilting around the *a* axis. The violet and green arrows indicate the displacement of Nd and Ba atoms, respectively. The red arrows in (b) and (d) indicate the shifting of the O1 atom along the *b* axis. In the *C*2*mm* phase, the MnO_6 octahedron has two nonequivalent Mn-O5 distances. In the *Cmmm* phase, two Mn-O5 distances in the MnO_6 octahedron are equal. Here, *m* indicates the mirror symmetry parallel to the view direction.

the presence of mirror symmetry perpendicular to the *a* axis as indicated by the arrowheads as shown in Fig. 2(b). It is worth noting that the CBED patterns observed from all segments at [100] incidence are similar and exhibit 2*mm* symmetry.

The observed symmetries of the CBED patterns from segment I and segment III(A1) indicate that the structure lacks mirror symmetry perpendicular to the *a* axis, which is in good agreement with polar space group *C*2*mm* (No. 38) reported in Ref. [19]. On the other hand, the observed symmetries of the CBED patterns from segment II and segment III(A2) indicate that the structure belongs to the nonpolar space group *Cmmm* (No. 65), exhibiting a mirror symmetry perpendicular to the *a* axis. Although the symmetries of the CBED patterns at [001] and [010] incidences for the *C*2*mm* phase differ from those of the *Cmmm* phase, as shown in Figs. 1 and 2, the corresponding SAED patterns are similar. The SAED patterns from the two phases cannot be distinguished from each other under the same experimental conditions, indicating that the lattice parameters of the *C*2*mm* and *Cmmm* structural phases are not significantly different. It should be noted that during examining 300 CBED patterns from 20 segments, the majority of the segments (≈90%) exhibit *C*2*mm* symmetry, while a limited number of the segments (≈10%) exhibit *Cmmm* symmetry. Therefore, the *C*2*mm* phase is expected to be the major phase of $NdBaMn_2O_6$ at RT, and *Cmmm* is the minor phase. Although the CBED patterns from a small number of specimen segments indicate the coexistence of both *C*2*mm* and *Cmmm* phases in the same segment, it is difficult to observe a clear domain boundary from the TEM image, as shown in Fig. S2(c) [25]. In this case, the four-dimensional (4D) scanning TEM (4D-STEM) imaging method, which is appropriate to examine the distribution of the two symmetry regions, can be a potential way to observe the domain boundary. As a segment with two phases simultaneously is rarely observed, the domain size is expected to be more than 100 μm.

Several model structures were constructed prior to structure optimization by estimating the atomic positions allowed by the determined space group. For the *C*2*mm* and *Cmmm* structural phases, 30 and 34 distinct model structures, respectively, were generated from the different combinations of the Nd, Ba, Mn, and O positions. The initial crystal structures of the *C*2*mm* and *Cmmm* phases were relaxed by performing DFT calculations using the QUANTUM ESPRESSO package. After structure relaxation, the optimized structures of each structural phase were categorized into two groups: The first group showed no tilting of MnO_6 octahedra about the *a* axis as shown in Figs. 3(a) and 3(c), whereas the second group showed tilting of the MnO_6 octahedra about the *a* axis (alternative shift of O1 atoms along the *a* axis) as shown in Figs. 3(b) and 3(d). The competition of the tilting and no-tilting structures of $NdBaMn_2O_6$ could be due to the position of $NdBaMn_2O_6$ on the phase boundary, where the tilting and no-tilting structural groups compete with each other [14,16] as discussed in Fig. S10 [25]. As these two types of optimized geometries of the $NdBaMn_2O_6$ structure are energetically stable, it is difficult to select the best-optimized structure only from DFT calculations. To obtain the most reliable structures for the *C*2*mm* and *Cmmm* phases, the experimentally obtained CBED patterns at [001], [100], and [010] incidences are visually compared with the simulated CBED patterns using optimized structures OS-1, OS-2, OS-3, and OS-4. Figure 4 shows the comparison between experimental and simulated CBED patterns at [001] incidence for the *C*2*mm* phase, and for the *Cmmm* phase, the comparison is shown in Fig. S11 [25]. It is found that the simulated CBED patterns at [001] incidence using no-tilting structures OS-1 and OS-3 well reproduce the experimental CBED patterns, whereas the tilting structures OS-2 and OS-4 are far from the experimental patterns. Therefore, the optimized structures OS-1 and OS-3 with no tilting of MnO_6 octahedra are selected as reliable crystal structures of the experimentally observed *C*2*mm* and *Cmmm*

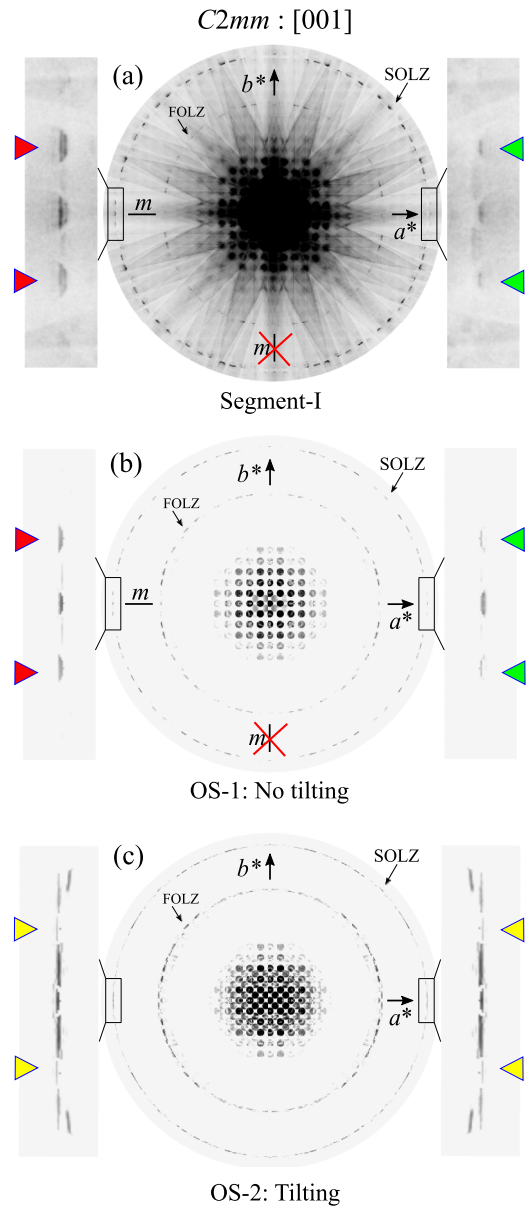

FIG. 4. Comparison between experimental and simulated CBED patterns at [001] of *C*2*mm* phase. Experimental CBED pattern at [001] incidence from (a) segment I. Simulated CBED patterns at [001] incidence using (b) OS-1 and (c) OS-2 optimized structures. Here, *m* indicates the mirror symmetry parallel to electron incidence. Simulated CBED patterns. The thicknesses of both simulated CBED patterns are 650 Å.

phases, respectively. The DFT calculations show that the difference in total energy between OS-1 and OS-3 is negligible (differ by 0.1 meV/atom) as shown in Fig. S12 [25]. The comparable total energies of the *C*2*mm* and *Cmmm* structural phases could be the origin of their coexistence.

The crystal structure of the polar *C*2*mm* phase with no tilt of MnO_6 octahedra as shown in Fig. 3(a), agrees with the previous study [19]. The displacement of the Nd (Nd1 and Nd2) and Ba (Ba1 and Ba2) atoms along the *a* axis are in opposite directions. The displacements of the Mn (indicated by magenta arrowheads) and O atoms along the *a* axis destroy the symmetry in which the mirror plane crosses each Mn site perpendicular to the *a* axis, resulting in two different Mn-O5 distances. Such displacements of the Mn and O atoms can induce spontaneous polarization along the *a* axis, as indicated by the black arrow in Fig. 3(a). In the case of the nonpolar *Cmmm* phase, both Nd and Ba atoms are displaced in the same direction as shown in Fig. 3(c). The shifting of Mn and O atoms along the *a* axis is limited by the space group symmetry, resulting in Mn-O5 distances being equal. The polar *C*2*mm* structure can be distinguished from the nonpolar *Cmmm* structure by the absence of mirror symmetry perpendicular to the *a* axis in real space. The absence of mirror symmetry in the polar *C*2*mm* phase is due to the breakdown of inversion symmetry caused by the failure of Friedel's law as discussed in Fig. S13 [25]. The observation of similar CBED patterns for the *C*2*mm* and *Cmmm* phases at [100] incidence from several segments are compatible with similar projected structures for both phases in the [100] direction, as shown in Fig. S14 [25].

In conclusion, the crystal structures of coexisting polar and nonpolar phases have been investigated by combining CBED and first-principles DFT methods, with experimental CBED patterns visually compared with simulated CBED patterns. The combined method successfully determined the crystal structures of coexisting polar *C*2*mm* (No. 38) and nonpolar *Cmmm* (No. 65) phases of $NdBaMn_2O_6$ at RT, exhibiting no tilting of MnO_6 octahedra. The observed SAED patterns indicated that the lattice parameters of both phases were nearly same. The DFT calculations suggested that the comparable total energies of both phases could be the origin of their coexistence. As the CBED method is sensitive to atomic positions and the DFT structure optimization can predict energetically stable structures, comparing experimental and simulated CBED patterns can guide in selecting the most reliable crystal structure. Hence, the combination of CBED and DFT methods can be a powerful tool for analyzing the coexisting or mixing states of a material. The current strategy is expected to work not only with multiphase materials but also with locally deformed structures, such as domain boundaries and interfaces.

We would like to thank Masaki Ageishi for the careful maintenance of the JEM-2010FEF transmission electron microscope. M.S.I. acknowledges the Japanese Government (MEXT) Scholarship. This work is partly supported by JSPS KAKENHI Grants No. JP18H03674, No. JP18K18931, No. JP19K14623, No. JP20H05176, and No. JP22H04495 the Research Program of "Dynamic Alliance for Open Innovation Bridging Human, Environment and Materials" in "Network Joint Research Center for Materials and Devices," The Murata Science Foundation, The Mitsubishi Foundation, and JST PRESTO JPMJPR22AB, Japan.

[1] Y. Zhang, W. Jie, P. Chen, W. Liu, and J. Hao, Adv. Mater. **30**, 1707007 (2018).
[2] L. Li, L. Xie, and X. Pan, Rep. Prog. Phys. **82**, 126502 (2019).
[3] S. I. Shkuratov and C. S. Lynch, J. Mater. **8**, 739 (2022).
[4] P. S. Halasyamani and K. R. Poeppelmeier, Chem. Mater. **10**, 2753 (1998).
[5] H. Tampo, P. Fons, A. Yamada, K.-K. Kim, H. Shibata, K. Matsubara, S. Niki, H. Yoshikawa, and H. Kanie, Appl. Phys. Lett. **87**, 141904 (2005).
[6] D. M. Többens and S. Schorr, Semicond. Sci. Technol. **32**, 103002 (2017).
[7] P. Müller, Crystallogr. Rev. **15**, 57 (2009).
[8] M. Tanaka, R. Saito, and K. Tsuzuki, J. Phys. Soc. Jpn. **51**, 2635 (1982).
[9] M. Tanaka, H. Sekii, and K. Ohi, Jpn. J. Appl. Phys. **24**, 814 (1985).
[10] M. Tanaka, M. Terauchi, and T. Kaneyama, *Convergent-Beam Electron Diffraction II* (JEOL-Maruzen, Tokyo, 1988).
[11] M. Tanaka, *International Tables for Crystallography*, edited by U. Shumueli, 3rd ed. (IUCr, Springer, Dordrecht, 2008), Vol. B, pp. 307–356.
[12] F. Giustino, *Materials Modelling Using Density Functional Theory: Properties and Predictions*, 1st ed. (Oxford University Press, Oxford, U.K., 2014).
[13] T. Arima, D. Akahoshi, K. Oikawa, T. Kamiyama, M. Uchida, Y. Matsui, and Y. Tokura, Phys. Rev. B **66**, 140408(R) (2002).
[14] T. Nakajima, H. Kageyama, H. Yoshizawa, and Y. Ueda, J. Phys. Soc. Jpn. **71**, 2843 (2002).
[15] D. Akahoshi, M. Uchida, Y. Tomioka, T. Arima, Y. Matsui, and Y. Tokura, Phys. Rev. Lett. **90**, 177203 (2003).
[16] T. Nakajima and Y. Ueda, J. Alloys Compd. **383**, 135 (2004).
[17] S. Yamada, H. Sagayama, K. Higuchi, T. Sasaki, K. Sugimoto, and T. Arima, Phys. Rev. B **95**, 035101 (2017).
[18] J. Blasco, G. Subías, M. L. Sanjuán, J. L. García-Muñoz, F. Fauth, and J. García, Phys. Rev. B **103**, 064105 (2021).
[19] M. S. Islam, D. Morikawa, S. Yamada, B. Aryal, K. Tsuda, and M. Terauchi, Phys. Rev. B **105**, 174114 (2022).
[20] P. Hohenberg and W. Kohn, Phys. Rev. **136**, B864 (1964).
[21] W. Kohn and L. J. Sham, Phys. Rev. **140**, A1133 (1965).
[22] G. B. Bachelet, D. R. Hamann, and M. Schlüter, Phys. Rev. B **26**, 4199 (1982).
[23] P. Giannozzi, S. Baroni, N. Bonini, M. Calandra, R. Car, C. Cavazzoni, D. Ceresoli, G. L. Chiarotti, M. Cococcioni, I. Dabo *et al.*, J. Phys.: Condens. Matter **21**, 395502 (2009).
[24] H. J. Monkhorst and J. D. Pack, Phys. Rev. B **13**, 5188 (1976).
[25] See Supplemental Material at http://link.aps.org/supplemental/10.1103/PhysRevB.108.L060104 for details about the schematic representation of the CBED pattern, TEM images, and SAED patterns, CBED patterns taken from different

segments, surface normal issue in the symmetry breaking of CBED patterns, background of competition between tilting and no-tilting structures in $R\mathrm{BaMn_2O_6}$, comparison between experimental and simulated CBED patterns, position of $\mathrm{NdBaMn_2O_6}$ in the phase boundary, difference between polar $C2mm$ and nonpolar $Cmmm$ phases, projected optimized structures of $C2mm$ and $Cmmm$ phases in the [100] direction, difference between [010] and [100] incidences's CBED patterns, and crystal structures of $C2mm$ (OS-1) and $Cmmm$ (OS-3) structural phases.

[26] K. Tsuda and M. Tanaka, Acta Crystallogr., Sect. A **55**, 939 (1999).

[27] K. Tsuda, Y. Ogata, K. Takagi, T. Hashimoto, and M. Tanaka, Acta Crystallogr., Sect. A **58**, 514 (2002).

[28] Y. Ogata, K. Tsuda, and M. Tanaka, Acta Crystallogr., Sect. A **64**, 587 (2008).